Physics   Faculty Publications & Research

1995

Nuclear Rings and Mass Inflow in Hydrodynamic Simulations of Barred Galaxies

B. Glenn Piner
Whittier College, gpiner@whittier.edu

James M. Stone

Peter J. Teuben

Recommended Citation

NUCLEAR RINGS AND MASS INFLOW IN HYDRODYNAMIC SIMULATIONS OF BARRED GALAXIES

B. GLENN PINER, JAMES M. STONE, AND PETER J. TEUBEN
Department of Astronomy, University of Maryland, College Park, MD 20742
Received 1994 October 14; accepted 1995 February 28

ABSTRACT

We study the gas dynamics in barred galaxies using time-dependent hydrodynamic simulations. To achieve high resolution near the galaxy's center, the simulations are performed in cylindrical coordinates using a non-uniform radial grid. The gravitational potential of the bar is assumed to be time-independent and is modeled using a Ferrers ellipsoid. We find that the gas flow evolves to a quasi-steady state in roughly five bar orbits, and the general features of this steady state are similar to previous studies. However, we also find that if the gravitational potential has two inner Lindblad resonances, and if along the major and minor axes the extremum of the $\Omega - \kappa/2$ curve between these resonances is at the same radial position, then the gas flow forms a dense nuclear ring located at the position of the extremum, or approximately 1 kpc for the models studied here. These two requirements are met by most models which have low axial ratio, i.e., thick bars. We study the development, evolution, and properties of the nuclear rings observed in our simulations in detail. We also study the effect of the bar on mass inflow into the nucleus of the galaxy. We find this inflow is highest for models with high axial ratio, i.e., thin, bars (which do not produce nuclear rings), where we find mass inflows of 0.25 $M_\odot$ yr^{-1} into the inner 0.1 kpc.

Subject headings: galaxies: active — galaxies: kinematics and dynamics — galaxies: nuclei —
galaxies: starburst — galaxies: structure — methods: numerical

1. INTRODUCTION

The gas in barred galaxies has many interesting morphological and kinematic features. For example, many barred galaxies show dust lanes leaving the nucleus along the leading edge of the bar. These dust lanes have been interpreted as shocks in the gas flow. Observational evidence that supports this interpretation includes the observed velocity jumps across the dust lanes and enhanced radio emission from the dust lanes (see Athanassoula 1992b for a more detailed summary and references). Yet another interesting feature of many barred galaxies is a nuclear ring. These rings are the locations of strong density enhancements in the gas and increased star formation, and usually occur within 1 kpc of the nucleus. One of the best examples of a galaxy with a nuclear ring is NGC 1097 (Hummel, van der Hulst, & Keel 1987). Buta (1986) has compiled a sample of 30 barred galaxies containing nuclear rings and has found that rings are usually circular rather than elliptical. Extremely high gas densities are observed in nuclear rings; for example, Wild et al. (1992) have observed an average density of 10^4 cm^{-3} in the nuclear ring of M82. Elmegreen (1994) has shown, through a linear instability analysis including magnetic fields and gas self-gravity, that nuclear rings should continue to accrete gas until the point at which their density exceeds a critical value: $\rho_{crit} = 0.6\kappa^2/G$, where κ is the epicyclic frequency and G is the gravitational constant. Thereafter the ring is unstable to a burst of rapid star formation, forming a starburst galaxy. Another feature of barred galaxies worthy of study is the proposal that a bar forces gas into the nucleus, and that this mass inflow is a possible power source for some active galactic nuclei (AGNs) (Simkin, Su, & Schwarz 1980; Shlosman, Frank, & Begelman 1989).

Each of the above-mentioned features has been confirmed by at least one numerical study of the gas dynamics in barred spirals. Many hydrodynamic simulations—for example, those

presented by Athanassoula (1992b)—confirm that the dust lanes are associated with shocks in the gas flow. She investigates the problem of mass inflow by measuring the mass-averaged radial velocity inside the Lagrangian radius, and finds inflows on the order of -1 km s^{-1}. Athanassoula also conducts a rather exhaustive parameter space search to study the structure of the gas in many different barred potentials. However, she does not find evidence of nuclear rings in her simulations, possibly because of a lack of resolution near the center. Shaw et al. (1993) find that nuclear rings form in their "sticky particle" simulations, although they do not see the strong density enhancements at the observed locations of the dust lanes. They conclude that two inner Lindblad resonances (ILRs) are required to cause the formation of a nuclear ring. Friedli & Benz (1993) have studied bar-driven fueling using a three-dimensional combined N-body and smooth particle hydrodynamics approach. They find mean values for the gas accretion rate into the inner 1 kpc of the galaxy of between 0.2 and 7 $M_\odot$ yr^{-1} with values peaking up to 100 $M_\odot$ yr^{-1}, whereas they estimate that a gas accretion rate of between 0.1 and 1000 $M_\odot$ yr^{-1} is necessary to power an AGN.

In this work we study the gas dynamics in barred galaxies using a state-of-the-art grid-based hydrodynamics algorithm which is formulated in cylindrical coordinates to provide high resolution near the galaxy's center. The primary motivations for carrying out this project were to investigate the mechanism of bar-driven fueling by direct measurement of the mass inflow rate into a small area around the nucleus, and to study the morphological features of the gas (such as nuclear rings) in the inner regions of barred galaxies. This is the first such study to use a grid-based hydrodynamics algorithm formulated in cylindrical coordinates, and hence these simulations are ideal for studying phenomena occurring in the inner regions of the galaxy. For example, we are able to measure the mass inflow

rate into the inner 0.1 kpc of the galaxy (which is 10 times closer to the nucleus than the values quoted by Friedli & Benz 1993), while the peak resolution of our simulations at a distance of 0.1 kpc from the nucleus is 2 pc (which is 50 times higher than the resolution of Athanassoula's simulations at the same location).

This paper is organized as follows. In § 2 we discuss the numerical methods, in § 3 we give the gravitational potential used to describe the galaxy, in § 4 we present the results of our simulations, and in § 5 we present our conclusions.

2. NUMERICAL METHODS

We use the code CMHOG written in 1991 by one of us (J. M. S.) to compute all simulations presented here. CMHOG is an implementation of the piecewise parabolic method (PPM) algorithm in its Lagrangian remap formulation (Colella & Woodward 1984) for gas dynamics. The code solves the fluid equations in the following four steps:

1. Interpolates values of the variables at the zone edges of the fixed Eulerian grid.
2. Solves a Riemann problem to find the average velocity and pressure at the zone edge during the time step.
3. Uses this velocity to shift the grid into a Lagrangian frame of reference and update the fluid equations.
4. Interpolates the values of the variables at the zone edges of the Lagrangian zones and then remaps the variables back onto the fixed Eulerian grid.

All interpolations are third order (parabolic). The original version of this code has been used for a number of astrophysical applications, and has been extensively tested with, e.g., shock tubes, advection tests, and the strong shock test suite of Woodward & Colella (1984). The code required several major changes to make it suitable for simulating galaxies, including conversion to cylindrical coordinates, changing to an isothermal equation of state, and addition of new body forces. We will briefly describe each of these changes after first giving a general description of the simulation properties.

2.1. Simulation Properties

All simulations were carried out using a two-dimensional cylindrical grid which extends from 0.1 to 16 kpc in radius. The boundary at 16 kpc is reflecting, while the boundary at 0.1 kpc is outflow (mass which crosses the inner boundary is considered lost). The grid is staggered in r, so that the zones remain square throughout the grid (i.e., $\Delta r = r\Delta\phi$ everywhere on the grid). This implies that the resolution at the center is 160 times better than the resolution at the outer edge. The numerical viscosity will therefore be higher at the outer edge, but because of the PPM algorithm's intrinsically small numerical viscosity we find that it is still negligible (see § 2.2.3). The calculations were carried out on a half-plane constructed by making a cut through the origin along the bar major axis. We assume a reflection symmetry about the origin to obtain the solution over the entire 2π radians. We also rotate the grid at the pattern speed of the bar, so that the bar remains fixed on the grid.

All simulations were done at one of two different resolutions, which will hereafter be referred to as high and low resolution. Low-resolution runs have 67 radial zones by 40 angular zones and have a resolution of 8 pc at the inner boundary and 400 pc at the end of the bar. High-resolution runs have 251 radial zones by 154 angular zones and have a resolution of 2 pc at the inner boundary and 100 pc at the end of the bar. The high-

resolution run requires quite a large number of time steps, about 120,000, to complete a 2 Gyr run. This is due to the fact that the zones near the origin are very small, so the time required for gas to cross one of these zones is small also. The high-resolution run has a time resolution of about 17,000 yr per time step.

Each simulation is initialized by setting the gas density to be uniform everywhere and the gravitational potential to be axisymmetric. The gas is initialized to be orbiting at its circular velocity in this potential. The bar is then added in slowly, over a time of 1×10^8 yr (or half a bar revolution), while keeping the total mass of the system constant. The bar is added in this way in order to avoid the violent shocks which occur when the bar is suddenly introduced. The simulation is then carried out to a time of 2 Gyr, or 10 bar revolutions, by which time the gas behavior has stabilized. The sound speed is kept constant at 5 km s^{-1} during the simulation.

The initial surface density of the gas has been set equal to 10 $M_\odot$ pc^{-2} for all of the runs. This implies a total gas mass of $8 \times 10^9 M_\odot$, or a ratio of total gas mas to total stellar mass of 1/19. Since the stellar density is sharply peaked toward the center of the galaxy while the initial gas density is constant, the ratio of gas mass to stellar mass varies with radius. For example, between radii of 0.5 and 1.0 kpc, in the area of the nuclear ring, the initial ratio of gas mass to stellar mass is only 1/552.

2.2. Changes to the Code

2.2.1. Cylindrical Coordinates

A cylindrical grid has naturally high azimuthal resolution near the origin and coarser azimuthal resolution at large radii. Thus a cylindrical grid is most suitable for investigating phenomena occurring near the nucleus, where a Cartesian grid would require a large number of uniform zones to achieve comparable resolution. For example, our highest resolution run simulates a half-plane of a 16 kpc galaxy using approximately 40,000 zones. This gives us a resolution of 2 pc at the inner boundary (0.1 kpc). A uniform Cartesian grid would require $(32/0.002) \times (16/0.002) \approx 10^8$ zones to achieve the same resolution. Since the code performs optimally for square zones, we stagger the radial grid lines so that $\Delta r = r\Delta\phi$ throughout the grid.

A difficulty which arises when trying to use PPM in cylindrical coordinates is that in this method the fluid variables are defined as the volume-averaged values within the zones, while the PPM interpolations are based at the geometrical center of the zones. In Cartesian coordinates these two locations are the same, but in cylindrical coordinates the volume-averaged center in r is displaced toward larger radii from the geometrical center in r. We use the prescription given by Blondin & Lufkin (1993) to extend the PPM algorithm to cylindrical coordinates. With this extension, the truncation errors near coordinate singularities are substantially reduced but are not entirely eliminated. Thus, we avoid carrying the simulation all the way down to $r = 0$. Instead we set the inner boundary at 0.1 kpc, which is a large enough number of zones away from the origin (13 zones for our worst resolution) that truncation errors are avoided.

2.2.2. Isothermal Equation of State

The real multiphase interstellar medium is complex (e.g., McKee & Ostriker 1977) and would be difficult to model in a simulation of this sort. We assume that the large-scale morphological features in the gas will be approximated correctly if

we assume the galaxy contains an ideal isothermal gas. We have modified the PPM algorithm for an isothermal equation of state by independently developing a Riemann solver for an isothermal gas. This solver is identical to that described by Balsara (1993) for the Lagrangian plus remap version of PPM. We use the flattener described by Balsara (1993) to smooth postshock oscillations in strong, standing shocks which can arise as a result of the insufficient numerical viscosity.

2.2.3. Addition of Forces

In order to simulate the gas dynamics in barred galaxies in a rotating frame of reference, both pseudo- and gravitational forces had to be added to the code. Pseudo-forces are needed because of the cylindrical coordinate system. They correspond to the centripetal force felt by fluid elements moving along curvilinear grid lines.

The forces due to gravity were calculated from the fixed stellar potential discussed in the next section. Gas self-gravity is neglected in these simulations. Since the potential of the bar is constant in time, forces due to gravity need only be calculated once at the beginning of the simulation. We applied the forces by the same method as that used by the VH-1 (Virginia Hydrodynamics I) code (J. M. Blondin 1992, private communication). This involves knowing the forces at the center of the Eulerian zones and the centers of the Lagrangian zones so that the time-averaged force during the time step can be applied. Since the fluid variables are in general not known at the centers of the Lagrangian zones, we used linear interpolation to find gravity and the required velocities at these locations.

A number of test problems were run to check the validity of these three changes to the code. The radial outflow problem described by Blondin & Lufkin (1993) to check the radial advection was run, along with one- and two-dimensional cylindrical shock tubes. Another particularly relevant simulation is a galaxy of uniform density in Keplerian rotation in an axisymmetric potential. In this case the density should remain uniform throughout the run. This test was performed, and it was found that the density did remain approximately constant and that there was negligible mass inflow due to numerical viscosity across the inner boundary.

3. THE POTENTIAL

For these simulations we used the model of Athanassoula (1992a) to describe the gravitational potential. An extensive description of this potential, including many orbit plots, is given in this reference. The model contains three components: a disk, a bulge, and a bar. The disk is a Kuzmin-Toomre disk (Kuzmin 1956; Toomre 1963) of surface density

$$\sigma(r) = (v_0^2/2\pi Gr)(1 + r^2/r_0^2)^{-1.5} , \quad (1)$$

where the constants v_0 and r_0 are $v_0 = 200$ km s^{-1} and $r_0 = 14.1$ kpc. The bulge has a volume density of

$$\rho(r) = \rho_b(1 + r^2/r_b^2)^{-1.5} . \quad (2)$$

The parameters ρ_b and r_b, which describe the central density and the radius of the bulge, are set by the four input parameters to the potential as described below. The bar is described by a Ferrers ellipsoid oriented along the y-axis of volume density

$$\rho = \begin{cases} \rho_0(1 - g^2)^n & \text{for } g < 1 , \\ 0 & \text{elsewhere ,} \end{cases} \quad (3)$$

where $g^2 = y^2/a^2 + (x^2 + z^2)/b^2$ and x, y, and z are the Cartesian coordinates. The exponent n is equal to 1 for the standard model; we also consider models with $n = 2$. The semimajor axis of the bar is kept fixed at $a = 5$ kpc. The model can now be completely determined by setting the values of four input parameters and demanding that the total mass within 10 kpc be a constant. The four input parameters are the axial ratio a/b of the bar (where a and b are the semimajor and semiminor axes, respectively), the quadrupole moment of the bar Q_m, the Lagrangian or corotation radius r_L, and the central concentration $\rho_c = \rho_0 + \rho_b$.

These four parameters completely determine the model through the following steps: Given values for the four parameters a/b, Q_m, r_L, and ρ_c, and with fixed values for the semimajor axis a and exponent n of the density distribution of the bar, we first determine the mass of the bar, M_b, via

$$Q_m = M_b a^2[1 - (a/b)^{-2}]/(5 + 2n) . \quad (4)$$

The central density of the bar, ρ_0, is then given by inverting

$$M_b = 2^{2n+3}\pi ab^2\rho_0 \Gamma(n + 1)\Gamma(n + 2)/\Gamma(2n + 4) . \quad (5)$$

Since the sum of the bulge and bar central densities ρ_c is an input parameter, the bulge central density ρ_b is just $\rho_b = \rho_c - \rho_0$. The bulge scale length r_b is then found through the constraint that all models have the same total mass within 10 kpc.

Since there is a one-to-one correspondence between the Lagrangian radius and the pattern speed of the bar, setting the Lagrangian radius is equivalent to setting the bar pattern speed. The values of these four input parameters for the standard model are $a/b = 2.5$, $Q_m = 4.5 \times 10^{10}$ $M_\odot$ kpc^2, $r_L = 6.0$ kpc, and $\rho_c = 2.4 \times 10^{10}$ $M_\odot$ kpc^{-3}. A Lagrangian radius of 6 kpc implies a bar pattern speed of 33 km s^{-1} kpc^{-1}, or a bar revolution time of 1.9×10^8 yr.

Figure 1 shows a plot of some of the characteristics of this standard model potential. The plot of angular velocity versus radius shows the local $\Omega - \kappa/2$, Ω, and $\Omega + \kappa/2$ curves along the bar major axis (solid line) and the bar minor axis (dotted line). The ILRs occur where the horizontal line representing the pattern speed of the bar intersects the $\Omega - \kappa/2$ curve. Note that this standard model has two ILRs. The spike in the $\Omega - \kappa/2$ curve along the bar major axis at 5 kpc is due to the bar ending at this point. It is somewhat softened if an $n = 2$ bar is used.

The density distributions for the three components of this model can be integrated to get a mass for each component. The total mass of each component interior to 16 kpc for the standard model is 4.1×10^{10} $M_\odot$ for the bulge, 9.8×10^{10} $M_\odot$ for the disk, and 1.5×10^{10} $M_\odot$ for the bar. This gives a total mass interior to 16 kpc of 1.54×10^{11} $M_\odot$.

4. RESULTS

Table 1 gives pertinent data for all the runs discussed in this paper. Missing identification numbers refer to runs which are not important for topics discussed in this paper. One of the runs (run 2) was carried out to a time of 4 Gyr to ensure that the 2 Gyr cutoff was indeed adequate. Another of the runs (Run 1) also included an equation designed to mimic gas recycling by density depletion due to star formation and density enhancement due to stellar mass loss. This will be discussed more in the following section. Before going on to present specific results regarding the nuclear rings and the mass inflow, we will first discuss some results for the standard model, which
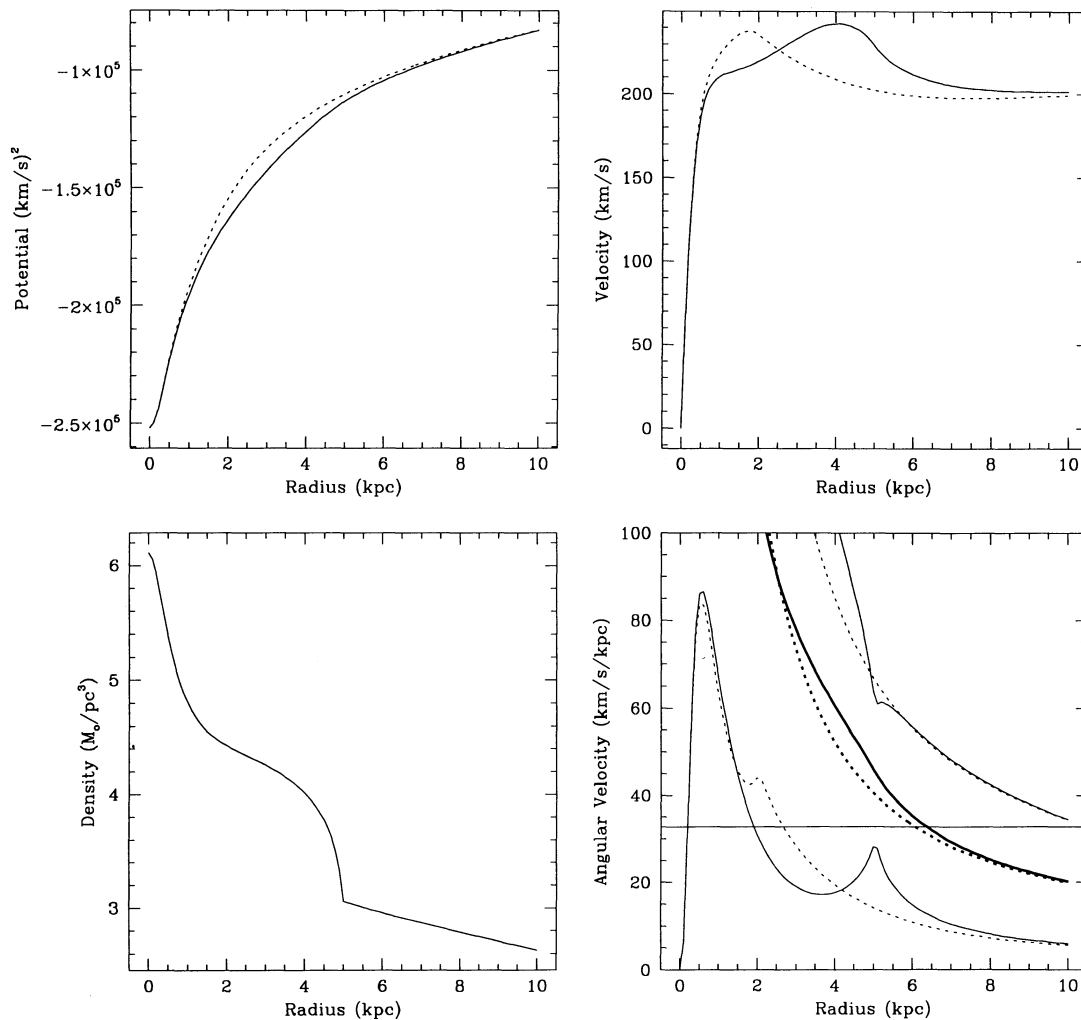
Fig. 1.—Standard model potential. Numerical parameters describing the standard model are given in § 3. In all four plots the solid line shows a slice along the bar major axis, while the dotted line shows a slice along the bar minor axis. (a) Gravitational potential vs. radius. (b) Rotational velocity in km s^{-1} vs. radius. (c) Stellar mass density vs. radius. (d) $\Omega + \kappa/2$ (*rightmost curves*), Ω (*middle curves*), and $\Omega - \kappa/2$ (*leftmost curves*), where Ω is the angular rotational velocity (km s^{-1} kpc^{-1}) and κ is the epicyclic frequency.

was defined in § 3 as having values for the four input parameters describing the potential of $a/b = 2.5$, $Q_m = 4.5 \times 10^{10}$ $M_\odot$ kpc^2, $r_L = 6.0$ kpc, and $\rho_c = 2.4 \times 10^{10}$ $M_\odot$ kpc^{-3}.

4.1. General Results for the High-Resolution Standard Model

Figure 2 shows some results from the high-resolution simulation at a time late in the run. Figure 2a shows a logarithmi-

cally scaled image of the gas density. The plot extends to 8 kpc on either side of the center, while the bar extends to 5 kpc on either side, so the entire bar is included. The bar is oriented vertically along the y-axis and is rotating in a counterclockwise direction. The density values saturate for a density about a factor of 75 higher than the initial density. The central black dot represents the inner boundary. At this point in the run the

TABLE 1

PARAMETERS OF THE SIMULATIONS

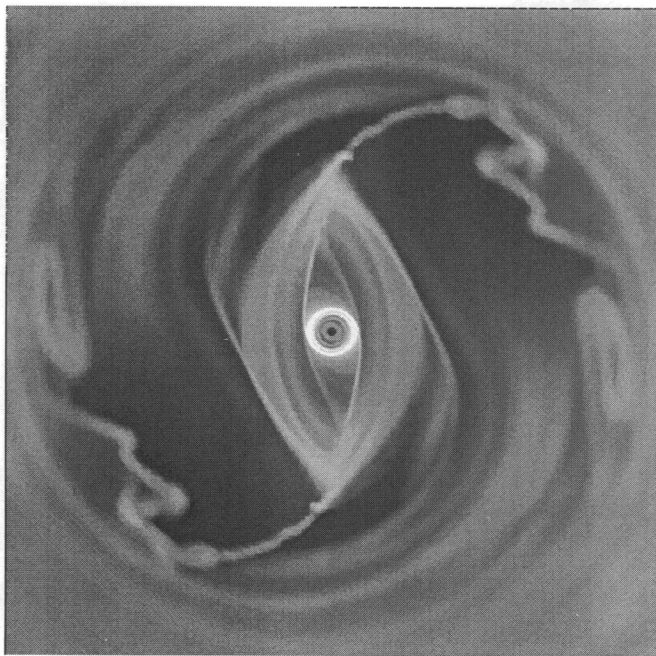| Identification	Resolution	Time[a] (Gyr)	n	a/b	Q_m (10^{10} $M_\odot$ kpc^2)	r_L (kpc)	ρ_c (10^{10} $M_\odot$ kpc^{-3})	Gas Recycling
1	Low	2	1	2.5	4.5	6.0	2.4	Yes
2	Low	4	1	2.5	4.5	6.0	2.4	No
4	High	2	1	2.5	4.5	6.0	2.4	No
8	Low	2	1	5.0	4.5	6.0	2.4	No
10	Low	2	1	2.5	4.5	6.0	0.8	No
11	Low	2	1	2.5	4.5	6.0	0.6	No
12	Low	2	1	2.5	4.5	6.0	0.4	No
14	Low	2	2	2.5	4.5	6.0	2.4	No

[a] Time at which simulation is stopped.
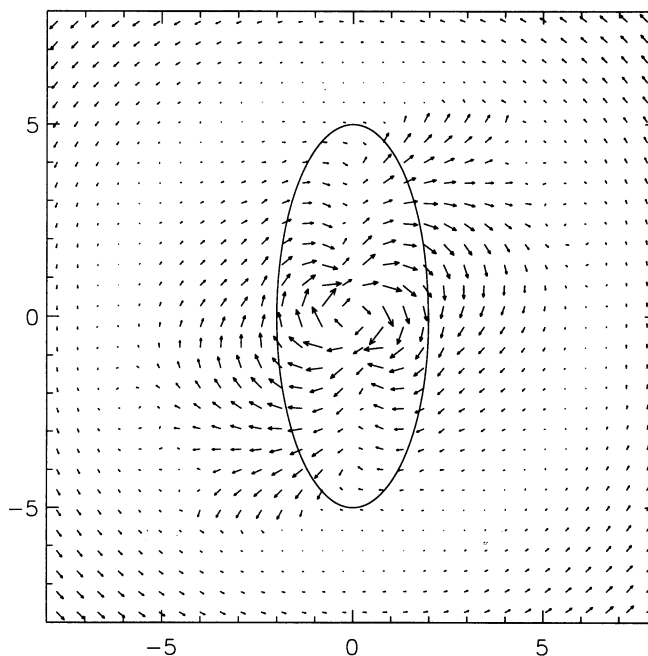
FIG. 2a

FIG. 2b

FIG. 2.—Results for the high-resolution standard model simulation. (a) Logarithmically scaled image of the gas density. The plot extends to 8 kpc on either side of the center, while the bar extends to 5 kpc on either side, so the entire bar is included. The bar is oriented vertically along the y-axis and is rotating in a counterclockwise direction. The density values saturate for a density about a factor of 75 higher than the initial density. Whiter colors indicate areas of higher density. (b) Velocity field in frame of reference rotating with the bar.

gas inside the bar has settled into a steady state. Due to hydrodynamic instabilities the gas flow directly outside the bar is not perfectly steady, but it does not show any major structural changes with the passage of time.

One of the most striking features on this image is the nuclear ring. Formation of the nuclear ring can be understood as an effect of the nonaxisymmetric potential of the bar. The bar potential produces a net torque on the gas which acts to drive the gas in toward the center (Schwarz 1981). In some potentials the gas settles into a nuclear ring between two ILRs; in other potentials it continues moving inward to the nucleus. Detailed properties of the nuclear ring in various potentials will be discussed in the next section. Other features are also clearly visible in Figure 2a. There are two narrow shocks which come out from the nuclear ring along the leading edge of the bar. These shocks, which are also evident in Athanassoula's simulations, can be identified with the observed locations of the dust lanes in real barred galaxies. The regions immediately surrounding the bar show a very low gas density, since here the gas has been swept up by the bar and is being funneled down into the nuclear ring. The narrow, dense streams of gas which emanate from each end of the bar major axis are disrupted into a complex flow at about the corotation radius. The reason for this can be seen in Figure 2b. This plot shows the velocity field in a frame of reference rotating with the bar. An outline of the bar has been overlaid on the plot to clarify its location. The corotation radius is easily visible as the point at which the velocity vectors have zero magnitude. It can be seen that the complex streams visible in Figure 2a occur at a location where the low-density gas is flowing outward and pushing on the higher density stream. This allows a Rayleigh-Taylor instability to develop. Moreover, the velocity shear present at the corotation radius causes the dense stream trailing from the bar

to become Kelvin-Helmholtz unstable as well. If the entire temporal evolution of the flow is viewed as a movie, the loops and whorls characteristic of these instabilities, and captured in this image, are clearly evident.

In order to illustrate the kinematics of the galaxy, in Figure 3 we plot contours of the different components of the velocity along different lines of sight. Figure 3a plots the contours of the x-velocity. Since the bar is aligned along the y-axis, this panel is appropriate to the case where the line of nodes is along the major axis of the bar. Figure 3b plots contours of the y-velocity, while Figure 3c shows the simulated radial velocity contours for a galaxy where the bar has been rotated through an angle of 45° from its previous alignment along the y-axis, and the galaxy has been inclined at an angle of 30° to the plane of the sky.

To verify that the nuclear ring is a physically meaningful result caused by the form of the gravitational potential, and not merely a numerical artifact, we have varied the numerical parameters of the simulations in a number of ways. For example, we find that the ring occurs at the same physical location when the position of the inner boundary is changed, and also when the boundary conditions specifying the rotational velocity across the inner boundary are changed. Several different boundary conditions were tried, including setting the rotational velocity in the boundary zones equal to the circular velocity, setting the rotational velocity to zero, and using linear extrapolation from the zones outside the boundary. These changes had negligible effect on the mass inflow. The ring occurs for bars with an exponent of $n = 2$, and the ring is stable over timescales as long as 4 Gyr. We also find that the ring does not occur in the same radial zone when the resolution is changed. In the low-resolution run the center of the ring is in the 29th zone at $r = 0.87$ kpc, while in the high-resolution run
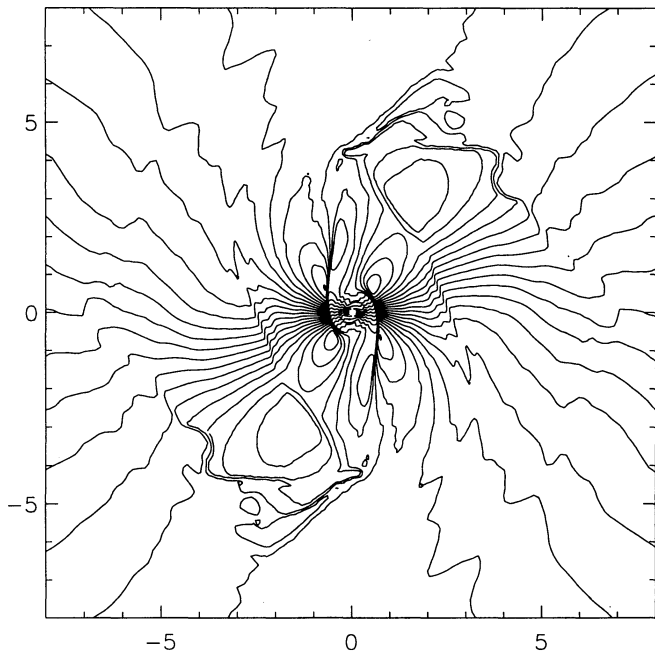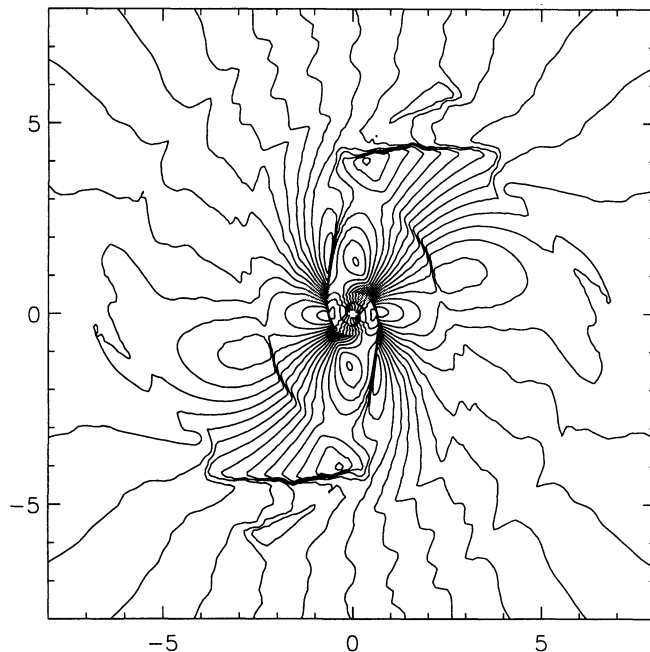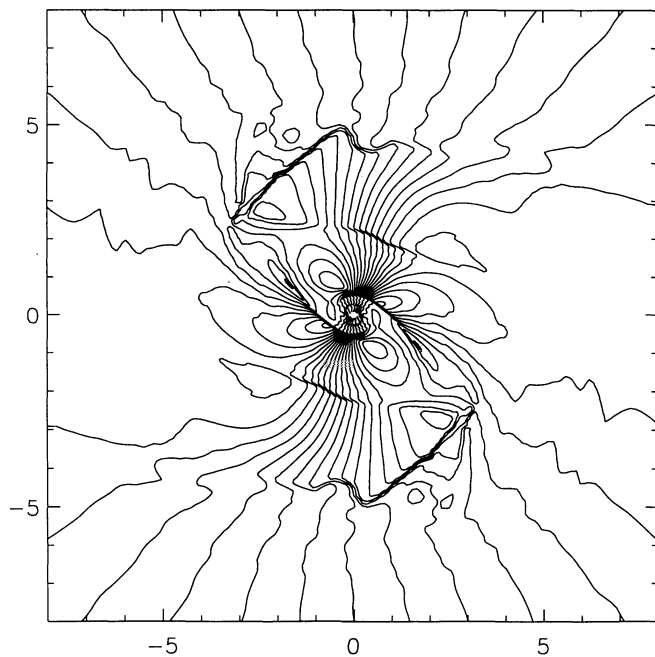
FIG. 3a

FIG. 3b

FIG. 3c

FIG. 3.—Contours of (a) x-velocities and (b) y-velocities in the plane of the galaxy. The bar is aligned along the y-axis. (c) Simulated radial velocity contours for a galaxy where the bar has been rotated through an angle of 45° from its previous alignment along the y-axis, and the galaxy has been inclined at an angle of 30° to the plane of the sky.

the center of the ring is in the 82d zone at $r = 0.51$ kpc. The center of the ring does move closer to the peak of the $\Omega - \kappa/2$ curve with higher resolution, as is expected. We have found that the only thing which drastically alters the ring is changing the gravitational potential; therefore we conclude that ring formation is due to the form of the potential.

The densities and masses given for the nuclear rings in the following section do not include the effects of gas recycling. They must therefore be considered as overestimates, because in a real galaxy stars will form in high gas density regions more efficiently than they will form in low gas density regions, thus lessening the high-density contrasts seen in the ring. In one of the runs with a potential identical to the standard model, gas recycling was mimicked by (Athanassoula 1992b)

$$d\rho/dt = \alpha(\rho_i^2 - \rho^2) , \qquad (6)$$

where ρ is the density of gas in the zone, ρ_i is the initial gas density of 10 $M_\odot$ pc^{-2}, and α is a constant equal to 0.03 pc^2 $M_\odot^{-1}$ Gyr^{-1}. This equation lowers gas density in zones where it is high, which mimics star formation, and also adds gas uniformly over the grid, which mimics stellar mass loss. The constant α sets the timescale for all of the gas to be recycled. With α equal to 0.03 it will take $\sim 1/(\alpha\rho_i) = 3.3$ Gyr for all of the gas to be recycled.

The gas recycling equation had a rather large effect on high-density regions, as was expected. Gas densities in the nuclear ring went down by about a factor of 5 in the run with the recycling equation included, as compared with the same run without the recycling equation. Even though the recycling equation had a rather large effect, it was not included in the other runs. As noted by Athanassoula (1992b), equation (6) is only a rough estimate of gas recycling which attempts to parameterize the complex processes of both star formation and stellar mass loss. In this study, we choose to focus on the fundamental fluid dynamical processes in barred galaxies without the influence of other parameterized phenomena. The recycling equation can also cause a spuriously high value for the mass inflow discussed in § 4.3. The important point to remember is that since gas recycling was not included, the density contrasts in our results should be considered as upper limits.

4.2. Nuclear Rings

By far the most striking feature in the density image of Figure 2 is the nuclear ring. These rings are observed at various

radii, shapes, and strengths in many of the simulations we have run. Figure 4 shows a logarithmically scaled image of the gas density extending to 1 kpc on either side of the nucleus for the high-resolution standard model. The bar is again oriented vertically. The structure of the nuclear ring is easily resolved, and it can be seen that the nuclear ring has a rich structure and actually resembles a tightly wrapped spiral. By varying the form of our potential, we have been able to pin down two characteristics that our model galaxy must have in order to form a nuclear ring. These characteristics are the following:

1. The galaxy must have two inner Lindblad resonances.
2. The extrema of the $\Omega - \kappa/2$ curves along the major and minor axes between the resonances must be at the same radial position. Figure 1d shows an example where the extrema are at

the same radial position, while Figure 8 shows a counterexample where the extrema are slightly offset.

In order to test the first characteristic, we have lowered the central concentration of the galaxy until the ILRs disappear. In order to test the second characteristic, we have raised the axial ratio of the bar until the peak of the $\Omega - \kappa/2$ curve along the bar minor axis shifts noticeably compared with the peak along the bar major axis. These tests will be discussed in detail in the following subsections.

Table 2 lists data on the nuclear rings for selected simulations. The time evolution of the ring is given for the high-resolution run, and a coarse time evolution is listed for the identical potential low-resolution run. For all other runs, ring data are given for the ring in the state that it was in at the end
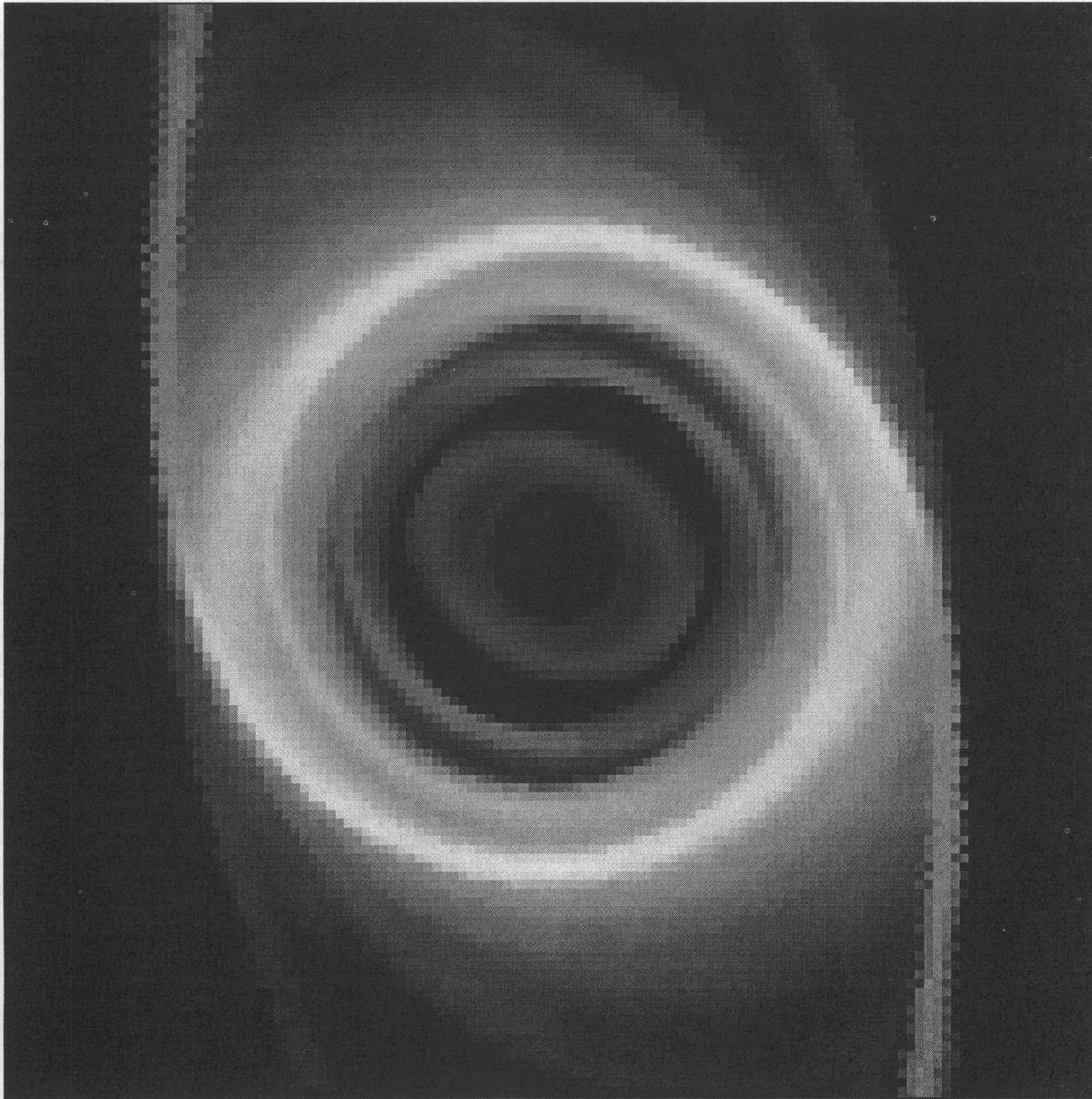

FIG. 4.—Logarithmically scaled image of the gas density showing a closeup of the nuclear regions for the high-resolution standard model. The plot extends to 1 kpc on either side of the center. The bar is oriented vertically. The internal structure of the nuclear ring is resolved in this figure.

TABLE 2

NUCLEAR RING DATA

Run	Time (Gyr)	r_a [a] (kpc)	r_b [b] (kpc)	Edges[c] (kpc)	M_{gas} [d] $10^9 M_\odot$	ρ_r/ρ_i [e]	ρ_{max}/ρ_i [f]	M_{st} [g] ($10^9 M_\odot$)	M_{gas}/M_{st}
1......	2.0	0.78	0.85	0.5, 1.1	0.15	5	12	16	1/107
2......	0.4	0.79	0.88	0.4, 1.2	0.32	8	21	21	1/66
	2.0	0.83	0.90	0.4, 1.3	1.0	21	50	23	1/23
	4.0	0.83	0.90	0.4, 1.35	1.4	27	61	24	1/17
4......	0.4	0.68	0.84	0.5, 1.0	0.25	11	66	13	1/52
	0.8	0.65	0.70	0.5, 0.8	0.31	25	135	8.0	1/26
	1.2	0.60	0.61	0.45, 0.7	0.40	44	186	6.8	1/17
	1.6	0.54	0.57	0.4, 0.7	0.53	51	207	8.2	1/15
	2.0	0.51	0.52	0.4, 0.65	0.62	75	257	6.8	1/11
10......	2.0	1.0	0.86	0.4, 1.3	0.20	4.2	16	23	1/113
14......	2.0	0.57	0.62	0.25, 1.0	1.2	41	85	19	1/16

[a] Location of ring center of mass along bar major axis.
[b] Location of ring center of mass along bar minor axis.
[c] Approximate inner and outer radii of ring.
[d] Mass of gas between inner and outer radii.
[e] Average increase in gas density in ring over initial density.
[f] Maximum gas density increase for single zone in ring.
[g] Mass of stars between inner and outer radii.

of the simulation. An important point to note is that in all cases the ring is situated between the two ILRs.

4.2.1. Time Evolution of the Ring at High Resolution for the Standard Model

The five lines listed for run 4 in Table 2 give the time evolution of the ring in steps of 0.4 Gyr for the high-resolution run. This time evolution is shown graphically in Figure 5. This figure shows the density as a function of radius at two slices through the ring. One slice is along the bar major axis (*solid line*), and the other slice is along the bar minor axis (*dotted line*).

Initially the ring is elliptical and is elongated along the bar minor axis. As time goes on, the ring loses its ellipticity and starts to become circular. The ring is approximately circular at a time of 1.2 Gyr. During this time the ring also moves inward and becomes narrower, denser, and more massive. The ring is not axisymmetric; there are azimuthal density variations within the ring of factors of 3, with the highest densities occurring along the bar major axis. At the end of the run the inward motion of the ring has slowed down, and it appears to have stabilized at about 0.5 kpc. This is to be expected, since we would not expect the ring to move past the extremum of the $\Omega - \kappa/2$ curves located at 0.5 kpc.

The ring also becomes more dense with time. This is due to two effects. The first effect is that the ring is both moving inward and becoming narrower, thus occupying a smaller area. The second effect is that at the same time mass is still being accreted onto the ring from the rest of the galaxy. At the end of the simulation the mass of the ring is $6.2 \times 10^8 M_\odot$, and the gas-to-stars mass ratio inside the ring is 1/11. This would be massive enough to start having an effect on the stellar orbits; the potential becomes more axisymmetric, and to first order more phase space will be available (van Albada & Sanders 1982) for the orbital family that the gas ring occupies (x_2; see, e.g., Contopoulos & Papayannopoulos 1980).

4.2.2. Central Concentration Comparison

In order to test the idea that ring formation is linked to the presence of ILRs, we have varied the input parameters so that the resonances disappeared. The resonances can be made to disappear by varying either the Lagrangian radius or the central concentration. Varying the Lagrangian radius is equivalent to varying the pattern speed of the bar. When the bar rotates fast enough, the peak of the $\Omega - \kappa/2$ curve is below the bar pattern speed and there are no ILRs. From the angular velocity curve of Figure 1, pattern speeds of more than 90 km s^{-1} kpc^{-1} will have no resonances. However, this high pattern speed would place the corotation radius at 2.5 kpc, well inside the bar. We wish to avoid such small values for the corotation radius, because according to Athanassoula (1992b) significant structural changes occur in the gas flow for values of the Lagrangian radius outside the range $r_L = 1.2a \pm 0.2a$; thus we choose to vary the central concentration instead.

When the central concentration is decreased, the rotational velocity in the inner kiloparsec of the galaxy is also decreased. Lowering the rotational velocity produces a lowering of the peak of the $\Omega - \kappa/2$ curve and will eventually lead to loss of the ILRs. The effect lowering the central concentration has on the resonances is shown in Figure 6, which shows plots of Ω, $\Omega + \kappa/2$, and $\Omega - \kappa/2$ along the bar major axis (*solid line*) and the bar minor axis (*dotted line*) for four different central concentrations. Figure 6a is for the standard central concentration of $2.4 \times 10^{10} M_\odot$ kpc^{-3}. The central concentration is then lowered through 8×10^9 (Fig. 6b) and 6×10^9 (Fig. 6c) to $4 \times 10^9 M_\odot$ kpc^{-3} (Fig. 6d). There are still two ILRs at a central concentration of 8×10^9, although the peak of the $\Omega - \kappa/2$ curve has been greatly reduced. At a central concentration of 6×10^9 there are just barely two ILRs. At 4×10^9 the $\Omega - \kappa/2$ curve along the bar major axis no longer intersects the bar pattern speed, and there are no ILRs.

Figure 7 shows logarithmically scaled density images for high-resolution simulations done with each of these central concentrations at a time of 2 Gyr. Images have the same linear and density scales as in Figure 2. The ring can be clearly seen to fade away as the central concentration is lowered. Data on the ring for the simulation with a central concentration of $8 \times 10^9 M_\odot$ kpc^{-3} are listed in Table 2 under run 10. The numbers given for mass and density clearly show the decrease in strength of the ring. The simulations at the two lowest central concentrations did not form nuclear rings. We can conclude from this that the ring will be stronger the higher the peak of the $\Omega - \kappa/2$ curve is above the pattern speed of the bar.
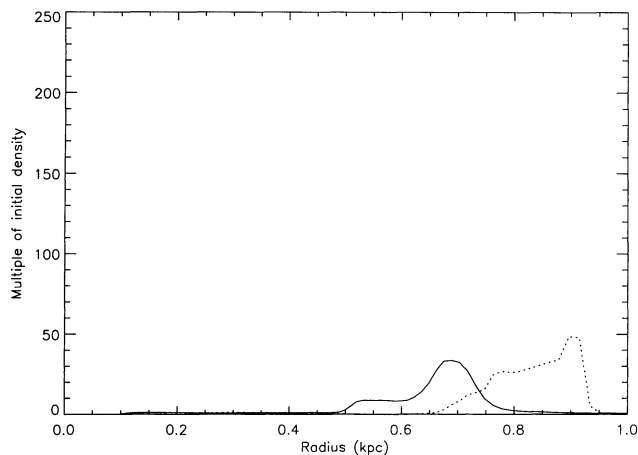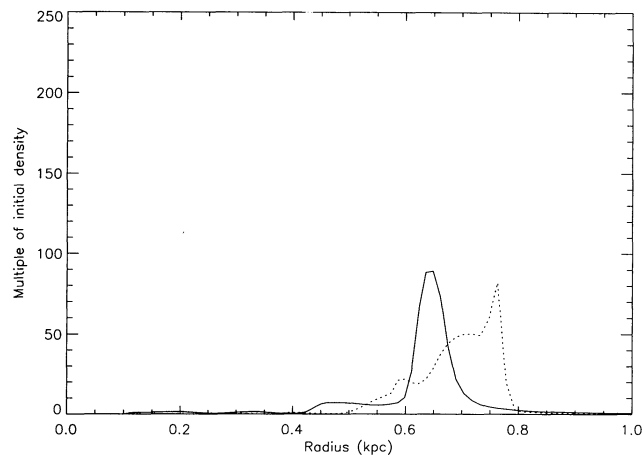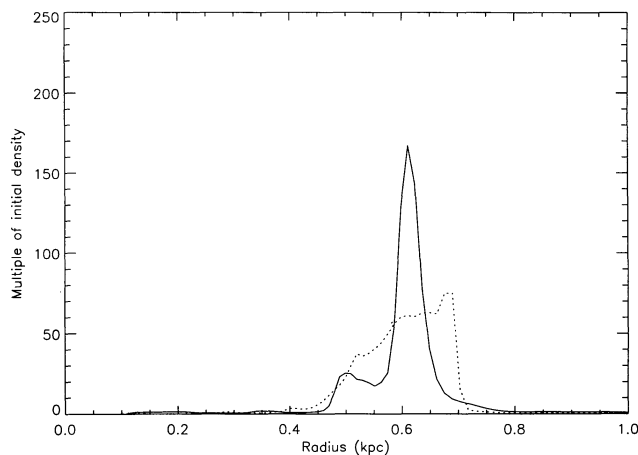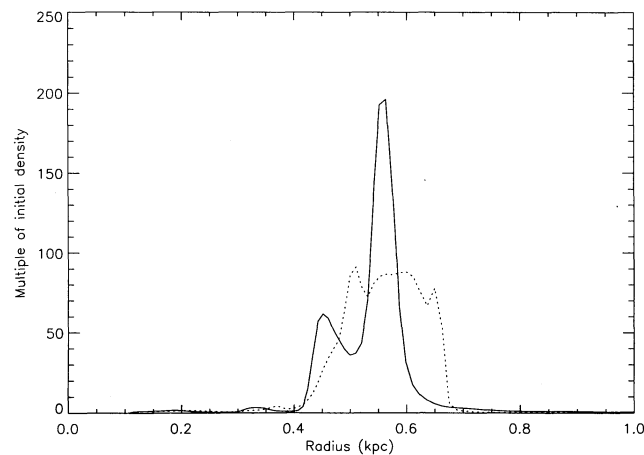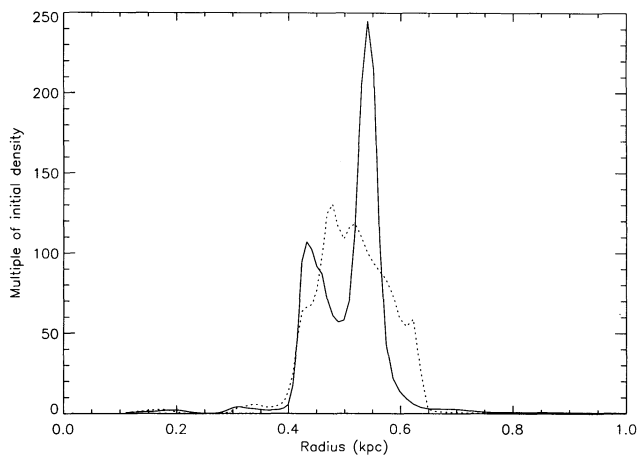
FIG. 5a

FIG. 5b

FIG. 5c

FIG. 5d

FIG. 5e

FIG. 5.—Time evolution of the nuclear ring for the high-resolution run: (a–e: t = 0.4, 0.8, 1.2, 1.6, and 2.0 Gyr, respectively). Solid lines show density cross sections along the bar major axis. Dotted lines show density cross sections along the bar minor axis.

Thus we expect galaxies with high central concentrations (i.e., galaxies that have bulges with high central densities and short radial scale lengths) to have strong nuclear rings. One interesting fact to note about the ring at a central concentration of $8 \times 10^9 \, M_\odot \, \mathrm{kpc}^{-3}$ is that it is elliptical and elongated in the direction of the bar major axis, unlike the standard model simulation at a central concentration of $2.4 \times 10^{10} \, M_\odot \, \mathrm{kpc}^{-3}$, where the ring is circular.

4.2.3. Axial Ratio and n = 2 Comparison

The simulations which investigate the effect of changing the axial ratio and the exponent of the density distribution of the bar were done at low resolution, so we must compare these with the standard model simulation at low resolution. The change from high to low resolution in the standard model does cause some changes in the ring, as can be seen in the entries for run 2 in Table 2. The important changes are that at low resolution the ring is broader, as we would expect for a lowered resolution, and it is consequently less dense.

Interestingly, when the axial ratio of the bar is raised from 2.5 to 5.0, the gas no longer settles into a nuclear ring but instead streams straight down into the nucleus. An image of
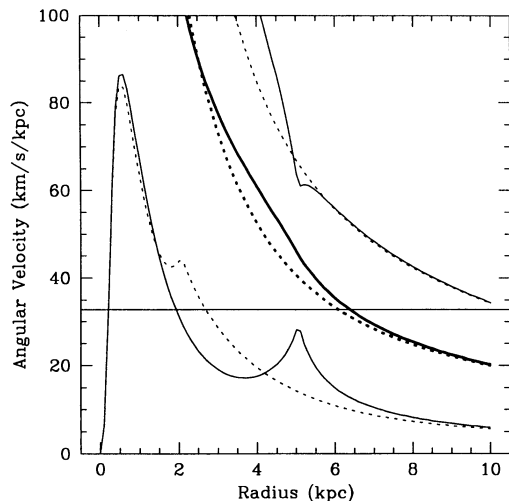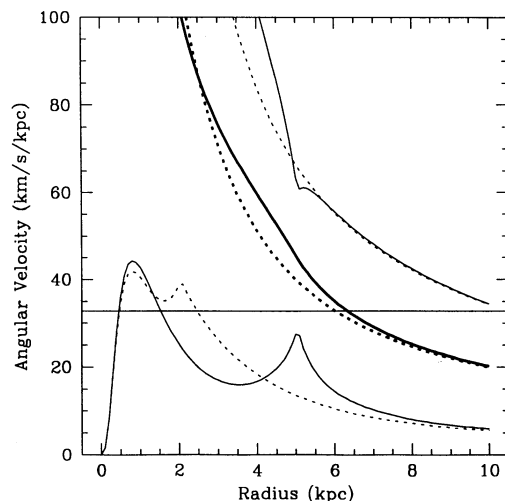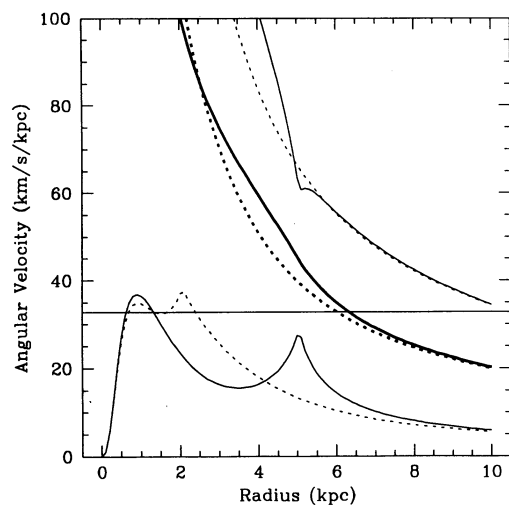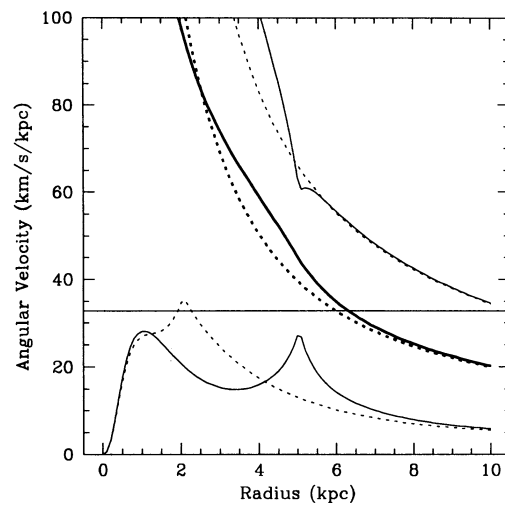
FIG. 6a

FIG. 6b

FIG. 6c

FIG. 6d

FIG. 6.—$\Omega + \kappa/2$ (*rightmost curves*), Ω (*middle curves*), and $\Omega - \kappa/2$ (*leftmost curves*) along the bar major axis (*solid line*), and along the bar minor axis (*dotted line*) for four different central concentrations (in units of $M_\odot$ kpc^{-3}). Ω is the angular rotational velocity (km s^{-1} kpc^{-1}), and κ is the epicyclic frequency. (a) $\rho_c = 2.4 \times 10^{10}$, (b) $\rho_c = 8 \times 10^9$, (c) $\rho_c = 6 \times 10^9$, (d) $\rho_c = 4 \times 10^9$.

the gas density, along with plots of Ω, $\Omega + \kappa/2$, and $\Omega - \kappa/2$ are shown in Figure 8 for this high axial ratio bar. The density image has the same linear and density scales as in Figure 2. The only important difference in the $\Omega - \kappa/2$ curve between this bar and the lower axial ratio bar (Fig. 1) is that for this bar the peak of the $\Omega - \kappa/2$ curve along the minor axis is shifted outward by about half a kiloparsec with respect to the peak of the curve along the major axis. Evidently this shift in the peaks of the $\Omega - \kappa/2$ curves makes it impossible for gas to settle into a ring formation between the resonances, and the gas falls down into the nucleus. Thus we expect nuclear rings to form only in galaxies with lower axial ratio bars.

We have also computed a simulation in which the exponent n in the formula for the bar density was equal to 2 instead of 1. This implies that the bar is more sharply peaked in density toward the center. The central density of this bar is greater than for the $n = 1$ bar, but falls off more rapidly with distance from the center. The ring formed in this case has moved inward

somewhat, is a bit narrower, is about twice as dense, and is slightly more massive than the comparable ring formed by the $n = 1$ bar. Evidently the $n = 2$ bar is more effective at trapping gas in a nuclear ring.

4.2.4. Critical Densities

It is interesting to compare the final density of the ring with the critical density for collapse predicted by Elmegreen (1994). Using the formula $\rho_{crit} = 0.6\kappa^2/G$, where $\kappa^2 = 4\Omega^2 + r\,d\Omega^2/dr$, $\Omega^2 = 1.4 \times 10^5$ s^{-2}, and $d\Omega^2/dr = -4.5 \times 10^5$ s^{-2} kpc^{-1} at $r = 0.5$ kpc, we obtain a value for the critical density of $\rho_{crit} = 47\ M_\odot$ pc^{-3} or $\rho_{crit} = 1900$ H atoms cm^{-3}. Assuming the gas has an exponential scale height of about 100 pc, our initial central volume density is 0.05 $M_\odot$ pc^{-3}. This implies that a density increase of roughly a factor of 1000 would reach the critical density.

None of the simulations come close to reaching such a large density increase. Even if the simulations were allowed to con-
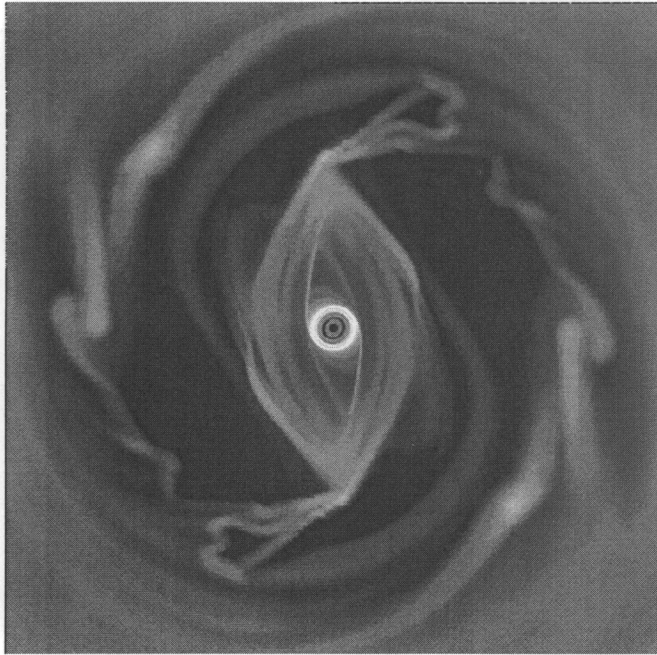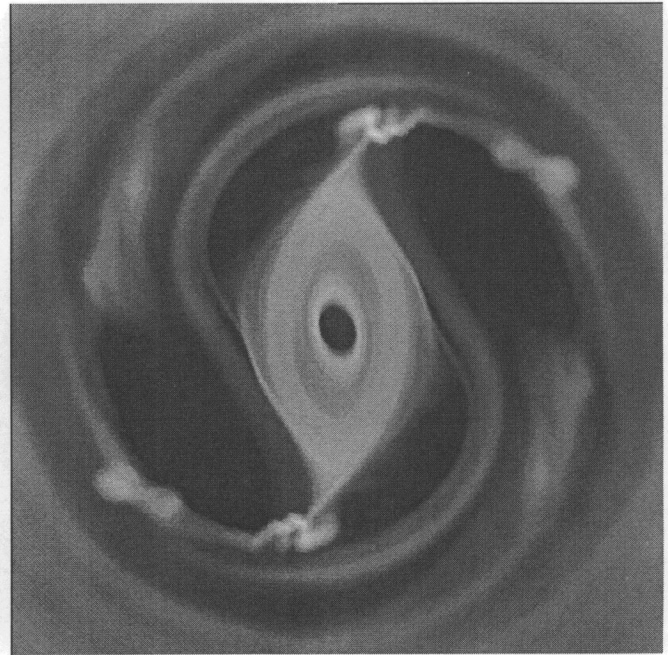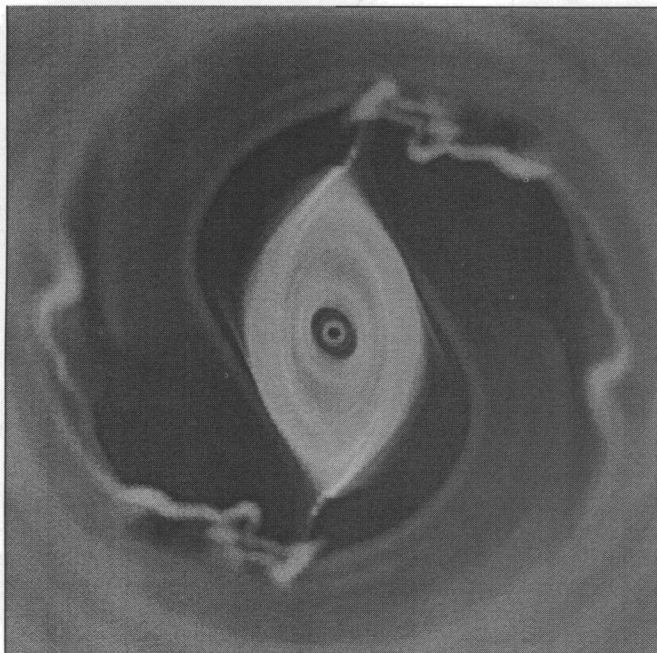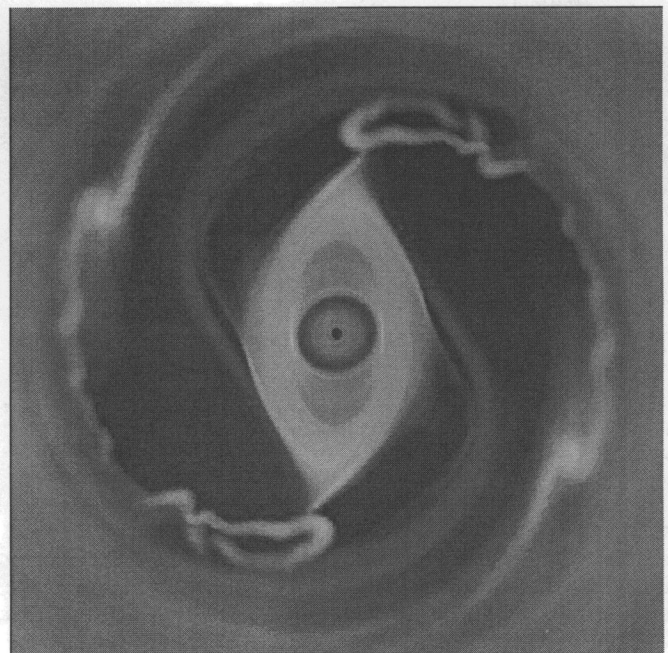
FIG. 7a

FIG. 7b

FIG. 7c

FIG. 7d

FIG. 7.—Logarithmically scaled images of gas density comparing four different central concentrations (units of $M_\odot$ kpc^{-3}). (a) $\rho_c = 2.4 \times 10^{10}$, (b) $\rho_c = 8 \times 10^9$, (c) $\rho_c = 6 \times 10^9$, (d) $\rho_c = 4 \times 10^9$. Images extend to the same distance from the center and have the same density scale as in Fig. 2.

tinue to run, the mass accretion rate onto the ring is slow enough that this density would not be reached in any reasonable amount of time. However, very high densities of this sort are observed in real starburst galaxies. For example, M82 has an average density of 10^4 cm^{-3} in its nuclear ring (Wild et al. 1992). Obviously something is causing much faster and stronger ring growth than we have observed in these simulations. Of course, these simulations have neglected cooling and gas

self-gravity. The inclusion of these factors would probably lead to more rapid ring growth.

4.3. Mass Inflow

The most accepted mechanism for creating the power observed in AGNs involves the accretion of matter onto a supermassive black hole at the galaxy's center. To create the observed luminosities requires a large rate of mass accretion. A
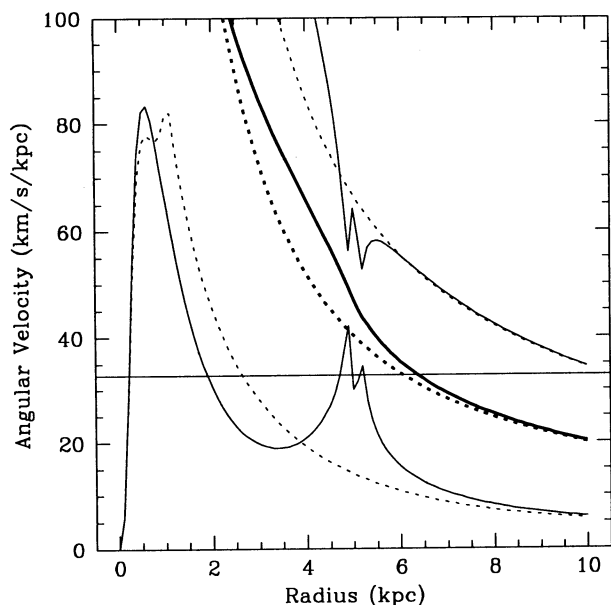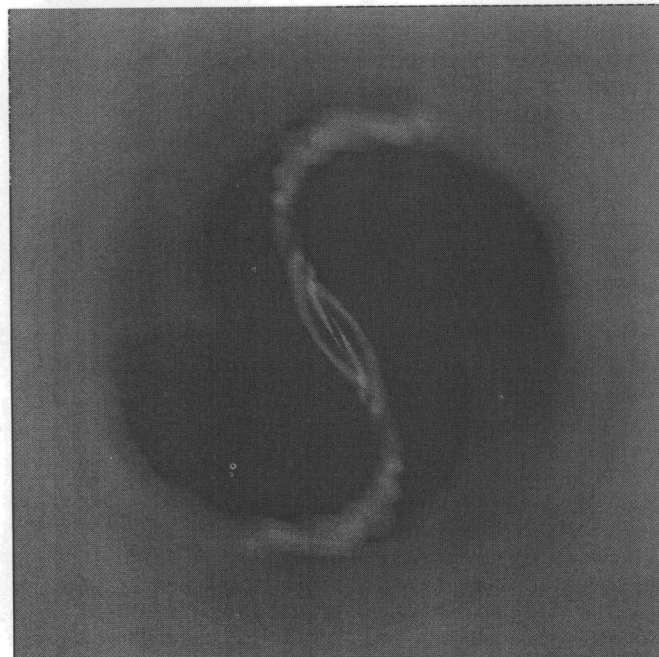
FIG. 8a

FIG. 8b

FIG. 8.—(a) $\Omega + \kappa/2$ (*rightmost curves*), Ω (*middle curves*), and $\Omega - \kappa/2$ (*leftmost curves*) along the bar major axis (*solid line*) and along the bar minor axis (*dotted line*) for the 5:1 axial ratio bar. Ω is the angular rotational velocity (km s^{-1} kpc^{-1}), and κ is the epicyclic frequency. (b) Density image for the 5:1 axial ratio bar. The image extends to the same distance from the center and has the same density scale as in Fig. 2.

proposed mechanism for generating this mass accretion supposes that a spinning bar causes gas to fall into the nucleus. We have tested this mechanism by measuring the rate of mass inflow into the inner 100 pc of the galaxy for each simulation.

The cylindrical grid which we employ makes this code ideal for studying this mass inflow phenomenon. Our numerical simulations use a circular inner boundary at a relatively small distance of 100 pc from the origin. The fact that this boundary is circular means that the flow around and through this boundary is smooth, which might not be the case for a rectangular boundary. Since the zones decrease in size toward the origin, we have excellent resolution in the nuclear regions.

When mass crosses this inner boundary, we assume it is lost to the simulation. In a real galaxy the buildup of large amounts of gas mass in the nucleus would eventually have some effect on the potential and would change both the gas flow patterns and the stellar orbits. We do not consider this effect here. Table 3 lists the measured mass inflow rates for each of the runs. The values quoted in Table 3 are for an initial gas density of 10 $M_\odot$ pc^{-2}. The mass inflow rate is directly proportional to the assumed value of the initial gas density.

TABLE 3
MASS INFLOW RATES

Identification	Inflow[a] ($M_\odot$ yr^{-1})	Identification	Inflow[a] ($M_\odot$ yr^{-1})
1.............	9.2×10^{-5}	10	2.7×10^{-6}
2.............	5.4×10^{-5}	11	9.4×10^{-5}
4.............	4.8×10^{-5}	12	9.5×10^{-5}
8.............	0.25	14	9.6×10^{-6}

[a] Average mass inflow through inner 100 pc after 1 Gyr ($M_\odot$ yr^{-1}).

There is a substantial inflow rate of about 5×10^{-5} $M_\odot$ yr^{-1} even from the standard model runs which form the nuclear rings (runs 2 and 4). There is a slight difference in mass inflow between runs 2 and 4 caused by the different resolutions. Evidently the nuclear ring is not really a true ring but more closely resembles a very tightly wrapped spiral. This is true in the sense that material enters the ring along the outer boundary and then eventually leaves again, crossing the ring inner boundary and heading toward the nucleus. Of course, the rate of mass leaving the ring is much slower than the ring's rate of mass accretion, which allows the ring to grow in mass and density. Although there is some mass inflow for these runs, the inflow is not sufficient to power any kind of AGN.

The values quoted for the mass inflow are the average values after 1 Gyr. The first gigayear of the simulation is ignored in order to give the galaxy a change to stabilize after the bar has been added. Figure 9 shows how the mass inflow rate changes with time for the standard model simulation carried out to 4 Gyr (run 2). The mass influx shows a sharp peak immediately after the bar is added and then slowly comes down to a constant value. From 1 to 4 Gyr, the mass flux then stays relatively constant.

Run 1 has a potential identical to that of runs 2 and 4, the only difference being that run 1 includes the gas recycling equation. When the recycling equation is included, the mass flux is about twice as high as when the equation is not included. This is because the recycling equation adds gas uniformly over the grid. Since mass is constantly being removed from the zone adjacent to the inner boundary anyway, this equation produces mass loading on the innermost zones and causes a higher mass flux across the inner boundary. Lowering the central concentration as was done for run 10, run 11, and run 12 produces a much lower mass inflow for run 10. This is due to two causes. The nuclear ring which forms in this run
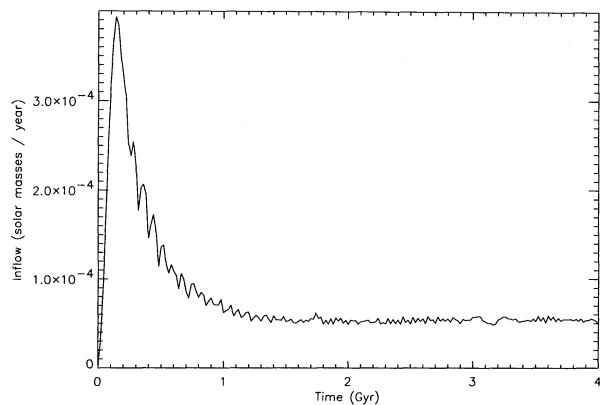
FIG. 9.—Mass flux entering the inner 100 pc for the 4 Gyr run (run 2)

keeps material from reaching the nucleus, and, since the central concentration is lower, material inside the ring is not strongly attracted to the nucleus anyway. Runs 11 and 12, which do not form nuclear rings, have relatively higher mass inflows, as would be expected. Run 14, which was run using a bar with an exponent of 2, has a significantly lower mass flux than the corresponding $n = 1$ run. An $n = 2$ bar is more sharply peaked in density toward the center and has a more dense and massive nuclear ring than the corresponding $n = 1$ run. These facts imply that gas has a harder time leaving the $n = 2$ ring and heading in toward the nucleus.

By far the most interesting entry in Table 3 is the entry for run 8, which had a very thin bar (5:1 axial ratio). The mass inflow for this case is about 5000 times higher than the corresponding run with a thick bar (2.5:1 axial ratio). The mass inflow rate is this high because a nuclear ring does not form with a 5:1 axial ratio bar (see § 4.2.3). Instead of getting trapped in a dense nuclear ring, the gas is free to stream directly down into the nucleus. A sustained gas accretion rate of $0.1\ M_\odot\ \mathrm{yr}^{-1} < \dot{M} < 1000\ M_\odot\ \mathrm{yr}^{-1}$ is necessary to power AGNs (Friedli & Benz 1993). This gas accretion rate of 0.25 $M_\odot\ \mathrm{yr}^{-1}$ should be sufficient to power a low-luminosity AGN.

The mass of gas in the entire galaxy is $8 \times 10^9\ M_\odot$, so if this inflow rate stays constant, then over a typical galaxy lifetime of 10 Gyr approximately one-third of the gas in the galaxy would have entered the nucleus. However, it is unlikely that this rate of mass inflow is kept up for that long a period of time. Friedli & Benz (1993) have calculated by coupled N-body and hydrodynamic simulations that once about $10^9\ M_\odot$ of gas has entered the nucleus, the gravitational potential is altered enough that the stellar orbits change and the bar is destroyed. So at the rate of mass inflow we observe in run 8, the bar-driven fueling would operate for about 4 Gyr until the bar was destroyed and mass accretion stopped. We can conclude from

these runs that bar-driven fueling is most effective in galaxies with thin (high axial ratio) bars. Galaxies with thicker bars tend to form nuclear rings, and these rings inhibit gas from reaching the nucleus. High axial ratio bars do not form rings, and the gas is instead driven into the nucleus.

Another way to characterize the mass inflow is to measure the mass-averaged radial velocity inside the Lagrangian radius. This number should be negative for net mass inflow. For the standard model runs with nuclear ring formation, we obtain values of about $-1\ \mathrm{km\ s}^{-1}$ for the mass-averaged radial velocity. This value agrees with previous values for the parameter given by Athanassoula. For the thin bar with the high mass inflow we obtain $-8\ \mathrm{km\ s}^{-1}$ for the mass-averaged radial velocity.

5. CONCLUSIONS

Several of the interesting phenomena which occur in barred galaxies are located in and around the nucleus. Two of these are the formation of nuclear rings and the powering of active nuclei by bar-driven fueling. We have studied both of these processes using a hydrodynamics code which is ideally suited for investigating the nuclear regions. The code is formulated in cylindrical coordinates giving excellent resolution near the center.

We found that there were two requirements the potential had to satisfy in order for a nuclear ring to form. These requirements are that a galaxy must have two ILRs and the extrema of the $\Omega - \kappa/2$ curves along the bar major and minor axes between the ILRs must be at the same radial position. These requirements are satisfied for centrally concentrated galaxies with low axial ratio bars. Thus we would expect nuclear rings to form in these systems. The only simulation which showed significant mass inflow into the nucleus was the simulation with the 5:1 axial ratio bar. This system had an inflow rate of 0.25 $M_\odot\ \mathrm{yr}^{-1}$, which is sufficient to power a low-luminosity AGN. Therefore, we conclude that bar-driven fueling is most effective in systems with high axial ratio bars.

This work could be extended in several interesting directions. We are currently trying to add a spiral potential off the end of the bar to investigate what effects spiral arms would have on the gas flow. It would also be interesting to do a full three-dimensional simulation so that the distribution of gas out of the galactic plane could be studied. And, of course, solving the barred galaxy problem exactly requires coupling an N-body code to the hydrodynamics code, so that the evolution of the stars and gas can be followed together.

REFERENCES

Athanassoula, E. 1992a, MNRAS, 259, 328
———. 1992b, MNRAS, 259, 345
Balsara, D. S. 1993, preprint
Blondin, J. M., & Lufkin, E. A. 1993, ApJS, 88, 589
Buta, R. 1986, ApJS, 61, 609
Colella, P., & Woodward, P. R. 1984, J. Comput. Phys., 54, 174
Contopoulos, G., & Papayannopoulos, T. 1980, A&A, 92, 33
Elmegreen, B. G. 1994, ApJ, 425, L73
Friedli, D., & Benz, W. 1993, A&A, 268, 65
Hummel, E., van der Hulst, J. M., & Keel, W. C. 1987, A&A, 172, 32
Kuzmin, G. 1956, Astron. Zh., 33, 27

McKee, C. F., & Ostriker, J. P. 1977, ApJ, 218, 148
Schwarz, M. P. 1981, ApJ, 247, 77
Shaw, M. A., Combes, F., Axon, D. J., & Wright, G. S. 1993, A&A, 273, 31
Shlosman, I., Frank, J., & Begelman, M. 1989, Nature, 338, 45
Simkin, S. M., Su, H. J., & Schwarz, M. P. 1980, ApJ, 237, 404
Toomre, A. 1963, ApJ, 138, 385
van Albada, T. S., & Sanders, R. H. 1982, MNRAS, 201, 303
Wild, W., Harris, A. I., Eckart, A., Genzel, R., Graf, U. U., Jackson, J. M., Russell, A. P. G., & Stutzki, J. 1992, A&A, 265, 44
Woodward, P. R., & Colella, P. 1984, J. Comput. Phys., 54, 115